Composite Optimization of a Wing Strut With Trailing Edge Morphing

Carrillo Córcoles, X.; Tsatsas, I.; Sodja, J.; De Breuker, R.

Important note
To cite this publication, please use the final published version (if applicable).
Please check the document version above.

Composite optimization of a wing strut with trailing edge morphing

Xavier Carrillo Córcoles[*], Ilias Tsatsas[†], Jurij Sodja[‡], and Roeland De Breuker [§]

High aspect ratio strut-braced wing aircraft can significantly reduce the induced drag while limiting the weight penalty of increasing the wingspan. As part of the Hybrid Electric Regional Wing Integration Novel Green Technologies (HERWINGT) project, a multifunctional morphing strut is being investigated. In this study, an optimization framework is proposed to define the thickness distribution of the morphing trailing edge of the strut to achieve the desired operational shapes while considering laminate manufacturing guidelines and material allowables. The optimizer finds designs capable of achieving the objective shapes and provides load and mass estimations that can be used to make design decisions. The output of the optimization will be used for the future detailed design, manufacturing and mechanical testing of a multi-functional strut demonstrator.

I. Introduction

In 2000, the European Commission set up the Advisory Council for Aviation Research and innovation in Europe (ACARE) to provide guidelines for Europe's aviation sector as a basis for moving the industry towards greener standards, increased industrial competitiveness and social benefits [1, 2]. With these objectives in mind, the European Union (EU) launched the Clean Sky Joint Undertaking and their successor programmes, Clean Sky 2 and Clean Aviation, tasked with the implementation of green and innovative technology development. The objectives of these programmes were clearly defined in both the Vision 2020 report from EASA [3] and the Flightpath 2050 report from the European Commission [4], which proposed the ambitious steps required to reduce the adverse effect of commercial air travel on the environment. With the latter report, the European Commission set the goal to achieve a 75% reduction in CO_2 emissions per passenger per kilometre, 90% reduction in NO_x and 65% reduction in perceived noise by 2050 with respect to aircraft available in the year 2000.

These objectives seem very ambitious for conventional aircraft design as it is becoming increasingly difficult to extract more performance out of the well-known wing and tube configuration. Therefore, unconventional designs are being investigated. One of the potential candidates to overcome these challenges is a Strut-Braced Wing (SBW), in which the strut provides a bending moment relief on the main wing, allowing an increase of the aspect ratio of the wing without the significant weight penalty of a conventional cantilevered wing. Consequently, the induced drag would be reduced [5], increasing the aerodynamic efficiency of the aircraft hence helping to reduce the emissions.

The SBW configuration has been extensively investigated by Virginia Tech Multidisciplinary Aircraft Design Group [6–10], whose work is also part of the Subsonic Ultra Green Aircraft Research (SUGAR) project led by The Boeing Company and studies an SBW aircraft as part of NASA N+3 concept studies [11]. Following these studies, within the Sustainable Flight Demonstrator (SFD) project [12], NASA and Boeing are developing the X-66, an experimental transonic truss-braced wing concept that could reduce the fuel consumption and the resulting emissions by up to 30% with respect to current commercial aircraft. Similarly, the University of Michigan investigated the aerodynamics of the SBW [13, 14], ONERA investigated the

---

[*]Researcher, Faculty of Aerospace Engineering, Aerospace Structures and Materials, Kluyverweg 1 2629 HS Delft, X.CarrilloCorcoles@tudelft.nl

[†]PhD Candidate, Faculty of Aerospace Engineering, Aerospace Structures and Materials, Kluyverweg 1 2629 HS Delft, I.Tsatsas@tudelft.nl

[‡]Assistant Professor, Faculty of Aerospace Engineering, Aerospace Structures and Materials, Kluyverweg 1 2629 HS Delft, J.Sodja@tudelft.nl, AIAA Senior Member

[§]Associate Professor, Faculty of Aerospace Engineering, Aerospace Structures and Materials, Kluyverweg 1 2629 HS Delft, R.deBreuker@tudelft.nl, AIAA Associate Fellow

concept in the ALBATROS research project[15], DLR in the FrEACs project [16] and, the European-funded project U-HARWARD [17] conducted different multidisciplinary analysis and concluded that even when using conservative assumptions, the SBW can substantially reduce the operational empty weight with respect to conventional wing-tube aircraft.

Now, the Hybrid Electric Regional Wing Integration Novel Green Technologies (HERWINGT) project in Clean Aviation is further investigating the SBW concept [18]. The objective of this project is to develop the key technologies to address a new design for a Hybrid Electric Regional Aircraft (HERA) maturing up to technology readiness level 5 (TRL5). Then, as part of the HERWINGT project, this study addresses the design of the morphing skin of the strut for future manufacturing and mechanical testing of a multi-functional demonstrator.

To do so, this study considers a morphing strut featuring the TRanslation Induced Camber(TRIC) principle [19, 20] developed at the Delft University of Technology. This concept introduces a cut along the span of the lower skin of the trailing edge (TE) and utilizes chordwise actuation to provide morphing capabilities, as represented in Figure 1. The actuator enforces a displacement such that the TE deflects up when the skin is pushed away from the spar and deflects down when it is actuated in the other direction. More detailed explanations of the working principles of the TRIC concept can be found in previous work [19, 20].

Finally, this study proposes a new optimization framework based on the framework developed in the MANTA project [21]. This framework is used to optimize the thickness distribution of the composite laminates of the skin such that the desired shapes can be achieved taking into account manufacturing guidelines, multiple load cases and material allowables.
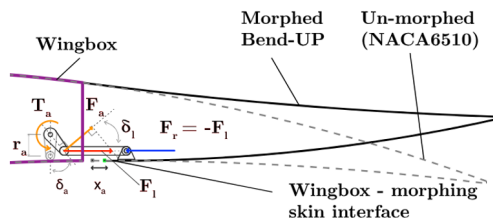

Fig. 1   Representation of the TRIC concept. Adopted from [20].

II. Optimization framework

The optimization framework is set up using the Bayesian Optimization (BO) algorithm in Matlab [22], which is connected to simulations running in Simcenter Nastran. In addition, PyNastran recovers the results from the simulations, which are then fed to the fitness function to evaluate each design. An overview of the different elements in this framework is presented in this section.

A. Finite Element Model

The simulations conducted within the optimization are solved in Simcenter Nastran [23] using a finite element model (FEM) built in Simcenter 3D [24]. For these simulations, the strutbox is considered rigid, hence the model is based on the TE geometry of the strut and represents a segment of the morphing strut, which will give an estimation of mass and loads per unit length of strut. For the final design, the strut is divided into spanwise modules that are actuated independently, as done in the TRIC concept [19, 20], which will allow for fine control of the aerodynamic shape.

The FEM represents the TE skin as Laminate 2D SHELL elements, from the rear spar at the upper skin to the slot at the lower skin. Furthermore, the skin is discretized in N regions in the chordwise direction, E_i, that can have different stacking sequences, which are used to achieve the objective shapes. The model is presented in Figure 2, showing the main features of the FEM in Figure 2a and the chordwise discretization in Figure 2b.

On the one hand, the TE skin is clamped at the top (CP in Figure 2), where it is connected to the spar. On the other hand, the actuator displacement is represented by an enforced displacement of the bottom end
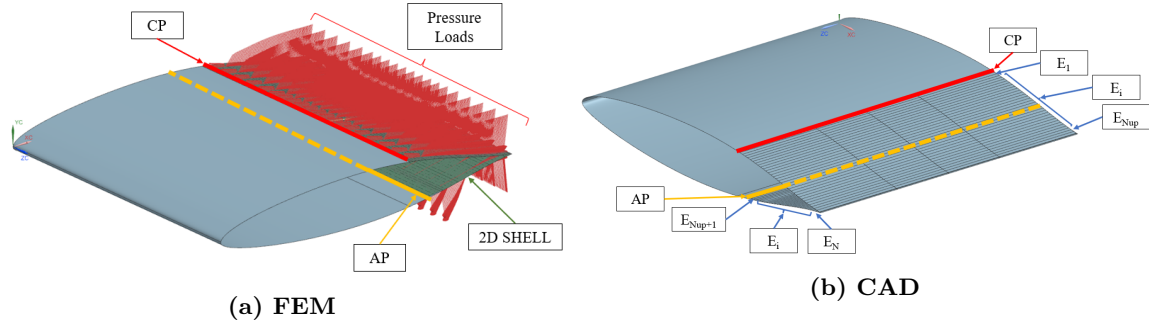
2

(a) FEM

(b) CAD

Fig. 2   Representation of the model used in Simcenter Nastran.

of the TE (AP in Figure 2) and a contact constraint, ensuring the tangency to the airfoil skin. In addition, the aerodynamic loads are included as pressure loads on the surface.

To conclude, different actuator displacements and aerodynamic loads are used to represent the load cases included in the optimization, which are presented in the following subsection. These load cases are solved using the linear static solution, SOL 101, and the results are recovered using PyNastran [25] to evaluate the fitness function.

B. Load cases

The optimization procedure can consider multiple load cases to size the morphing strut but three of them, considered the most relevant, are used in this study. The first is when the strut remains unmorphed, in which the skin has to be stiff enough to prevent bulging. Next, two limit cases are considered to better represent the operational envelope, one with positive deflection and one with negative deflection. These limit cases are defined considering both the aerodynamic studies [26] and preliminary structural analysis to define achievable deflections within the structural constraints. The aerodynamic loads corresponding to these load cases are provided by the aerodynamic study of the strut [26] and presented in Figure 3.
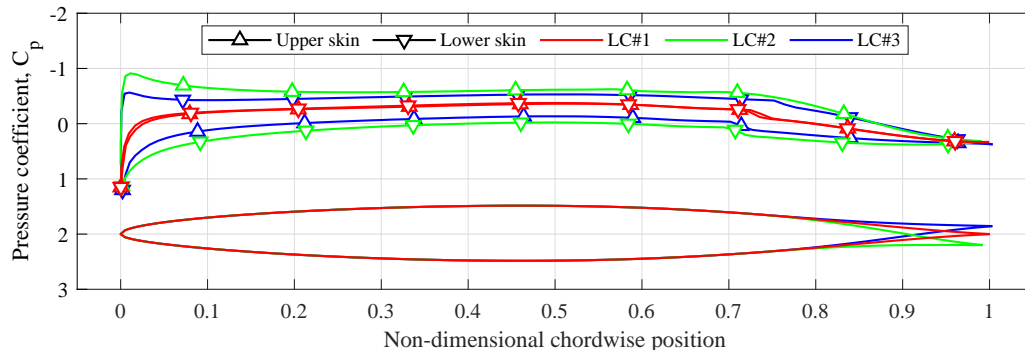

Fig. 3   Objective shapes and corresponding pressure coefficient distribution for each load case.

C. Objectives

The objective shapes, also shown in Figure 3, are provided by the project partners taking into account the type of morphing that will be implemented in the demonstrator. The TRIC concept provides the deflection of the trailing edge by increasing or decreasing the wetted length of the bottom skin, thus the length of the top skin has to remain constant. This constraint is enforced when optimizing the aerodynamic shapes. In addition, it is also desirable that the output design is as light as possible, hence the weight of the laminate is also accounted for in this framework.

3

D. Constraints

The design space is mainly constrained by manufacturing guidelines: (i) the laminate has to be symmetric and as balanced as possible, (ii) the plies should be dropped in the mid-plane instead of the outer surfaces, (iii) the ratio between ply thickness and the distance between ply drop-offs should be at least 1:20. In addition, two materials are considered: a carbon woven prepreg and a glass woven prepreg [27]. The properties of these materials are provided in Table 1.

Table 1   Composite material properties [27]

Parameter	T300JB Carbon Woven Prepreg	EC6 Glass Woven Prepreg
0° tensile modulus, GPa	55.9	21.2
90° tensile modulus, GPa	54.4	20.0
In-plane shear modulus, GPa	3.9	4.1
0° compressive strength, MPa	571	470
90° compressive strength, MPa	586	316
0° tensile strength, MPa	753	494
90° tensile strength, MPa	716	369
In-plane shear strength, MPa	124	98
Cured ply thickness, mm	0.23	0.24
Density, g/cm^3	1.55	1.95

Given these guidelines, the directions of the plies are limited to 0°/90° and ±45° to facilitate the laminate being balanced (i). Therefore, the possible stacking sequences are limited to alternating 0°/90° and ±45° plies, are enforced to be symmetric about the mid-plane (i) and they are dropped at the mid-plane (ii). Furthermore, the laminate chordwise discretization in N regions, E_i, of constant thickness, is chosen such that the distance between ply drop-offs is adequate (iii). In addition, only one ply can be dropped per element due to the design space that will be described in the next subsection, ensuring a smooth transition of thickness. Finally, the material strength is assessed using the maximum strain failure index from Nastran, including a safety factor (SF) of 1.5 to account for uncertainties.

E. Optimization problem

For the optimization problem, each design considered by the algorithm is defined by $N + A$ design variables, where N is the number of chordwise regions and A is the number of load cases.

The first N variables are integers used to define the number of plies of each region, which is the sum of the number of regions on the upper surface, N_{up}, and the number of regions on the lower surface, N_{low}. Then, n_1 and $n_{N_{up}+1}$ define the number of plies at the first regions on the upper and lower surfaces respectively. Next, the thickness of the subsequent regions is defined with the increase of plies between regions, n_i, which can be any value within $[-1, 0, 1]$. With this definition combined with the discretization and allowed laminate stacking sequences, all the manufacturing guidelines are ensured. To illustrate how each design corresponds to a thickness distribution, Table 2 presents the ply array, P, corresponding to an example design, $\mathbf{D}$, with $N_{up} = N_{low} = 5$ ($N = 10$).

Table 2   Example of design variable array with $N_{up} = N_{low} = 5$ ($N = 10$) and corresponding thickness distribution (plies).

Region , E_i	1	2	3	4	5	6	7	8	9	10
Example design, $\mathbf{D}$	16	-1	0	-1	1	7	1	1	0	-1
Ply array, P	16	15	15	14	15	7	8	9	9	8

In addition to the thickness definition, each load case includes a different number of actuation steps, a_i,

defined as integers. These variables are used to allow the optimizer to choose the best actuation displacement to achieve the objective shape.

Therefore, the array of variables defining each design would be:

$$\mathbf{x} = [n_1, ..., n_{N_{up}}, n_{N_{up}+1}, ..., n_N, a_1, ..., a_A] \tag{1}$$

Then, the optimization problem would be:

$$\min_{\mathbf{x}} \quad g(\mathbf{x}) \tag{2}$$

$$\text{subject to} \quad LB \le n_1, n_{N_{up}+1} \text{ [plies]} \le UB$$
$$n_i \text{ [Δplies]} = [-1, 0, 1]$$
$$a_{i,min} \le a_i \text{ [steps]} \le a_{i,max}$$
$$LB \le p_i \text{ [plies]} \le UB$$

where $g(x)$ is the fitness function presented later in this section, the boundaries for the actuator displacements are defined considering the initial deflection and the objective shapes, and the lower boundary (LB) and upper boundary (UB) for the laminate thickness are fixed to 6 and 20 plies respectively based on design requirements. Notice also that all the design variables are defined as integers for practical reasons when setting up the interface between the different software used in the framework.

Finally, as can be seen in Equation 2, none of the constraints accounts for the material allowables, the objective shapes or the weight of the design. This is because, due to the architecture of Matlab optimization functions, it is not efficient to evaluate the results of the simulation to compute both the fitness function and the constraints. For this reason, the objective shapes, the failure index constraint and the weight are incorporated into the fitness function as different penalties. The following sections present how each of these penalties is computed.

1. Objective shapes

For each load case, a different objective shape is provided based on the aerodynamic performance assessment [26]. Therefore, for every design and load case, the deflection is compared to the objectives to compute the penalty function related to the shapes. At the midline of the skin, an error function, $\epsilon(s)$, is defined as a function of the deflection, $\Delta U(s)$ and the objective deflection, $\Delta U_{obj}(s)$, along the lengthwise coordinate, s, of the midline:

$$\epsilon(s) = |\Delta U(s) - \Delta U_{obj}(s)| \tag{3}$$

It is then possible to integrate this error function to quantify how far is the deflection from the objective shape to obtain the penalty, F_i, corresponding to the shape of a given load case:

$$F_i = \frac{\int_0^1 \epsilon(s)}{C_i} \tag{4}$$

where C_i is a scaling factor to control the weights of these penalties within the objective function.

2. Strain failure index

The strain failure index (FI) is evaluated in a binary approach: when the failure index times the safety factor is higher than one, the penalty is applied to the objective function. Therefore, for each load case, the penalty related to the strain failure index, S_i, is defined as:

$$S_i = \begin{cases} 1 \text{ if } SF \cdot FI \ge 1 \\ 0 \text{ if } SF \cdot FI < 1 \end{cases} \tag{5}$$

Notice that with $SF = 1.5$, the maximum allowed FI is:

$$FI_{max} = \frac{1}{SF} \approx 0.66 \tag{6}$$

3. Mass minimization

The mass of the skins is proportional to the number of plies and the surface of the longitudinal regions. Given that all of the regions have the same width, their length, l_i, can be used to compute a weighted laminate thickness, which can be used as an indicator of the weight:

$$W = \frac{\sum_{i=1}^{N} l_i p_i}{C_W} \tag{7}$$

where C_W is a scaling factor based on the thickness of a morphing application of similar dimensions [20] and the length of the skin to be optimized. Similar to the objective functions, C_W is used to control the weight of the mass objective within the objective function.

4. Final implementation

The final objective function, $g(\mathbf{x})$, is a sum of the already presented penalties. In addition, it is a good practice to define the problem as a minimization problem with a negative minimum. Therefore, $g(\mathbf{x})$ is defined and normalized as:

$$g(\mathbf{x}) = \frac{-1 - 2A + \sum_{i=1}^{A} F_i + \sum_{i=1}^{A} S_i + W}{1 + 2A} \tag{8}$$

where the best result, in which all the penalties are equal to zero, would be:

$$g(\mathbf{x}) = -1 \tag{9}$$

III. Results

This section presents the results of the optimization procedure for both considered materials. The main outputs of this procedure are the thickness distribution and the different penalty values included in the objective function. However, to facilitate the comparison, these results are presented together with the post-processed results in Figure 4 and Table 3 respectively.

First, the optimization is conducted for each material, providing a thickness distribution and the fitness value corresponding to that design. Next, a sensitivity analysis is conducted around the optimal design: the number of plies at each region is decreased or increased by one at each of the design regions independently, providing a response surface to evaluate the optimality of the design. Finally, using the sensitivity information, the design is refined to remove unnecessary complex manufacturing features and improve the fitness if possible.

From the dashed lines in Figure 4, the optimization for both materials show similar trends in the thickness distribution. On the one hand, the upper skin has its thickest region close to the spar, the thickness is then reduced to the minimum allowed in the central region and it increases again at the trailing edge. This lower thickness region results in a skin acting as a compliant hinge, allowing a good match with the objective shapes. On the other hand, the lower skin presents two thicker regions, one at the trailing edge and one at the center of the skin. In addition, the carbon skin presents a third region with a higher thickness close to the spar. Finally, notice also that there are some zones of the laminate where the thickness increases or decreases for a single design region, showing a spike in the thickness distribution like the one at the spar region in the upper skin of the glass fiber design. This type of behaviour is related to the definition of the design variables and the use of a gradient-free optimizer like the BO algorithm. Therefore, it is important to study the sensitivity of the design such that unnecessary complexity is removed from the design, which is done in the *Post-Processing* step.

Focusing on the *Initial* designs in Table 3, both materials provide similar fitness results but the distribution of penalties is different. For both materials, none of the strength constraints is active, thus the related penalties, S_i are equal to zero. However, the design using carbon fiber provides lower shape penalties, F_i, and a higher mass penalty, W. Therefore, the carbon fiber design is better at matching the objective shapes than the glass fiber one, but it results in a higher thickness. This difference shows the sensitivity of the optimization to the weight of each penalty, emphasizing the importance of adapting the weights to the design objectives of each use case.

Next, using the *Initial* design as a starting point, Figure 5 presents a response surface to study the changes in the fitness function due to variations in the thickness of each region. Both materials present a
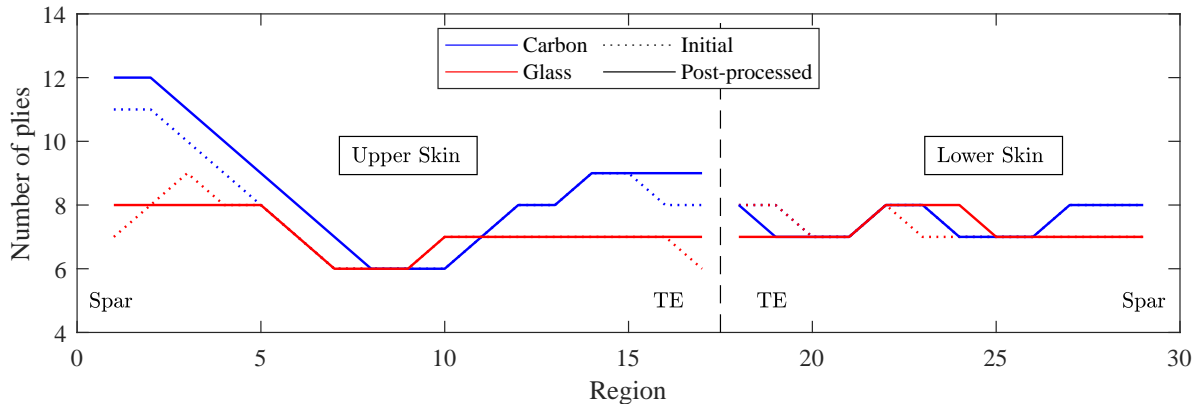
6

Fig. 4   Thickness distribution for each material and design.

**Table 3   Optimization penalties and fitness for each material**

Material	Design	$\mathbf{F}_1$	$\mathbf{F}_2$	$\mathbf{F}_3$	$\mathbf{S}_1$	$\mathbf{S}_2$	$\mathbf{S}_3$	$\mathbf{W}$	Fitness, $g(\mathbf{X})$
Carbon	Initial	0.243	0.544	0.545	0	0	0	0.562	-0.956
	Post-Processed	0.231	0.465	0.526	0	0	0	0.581	-0.957
Glass	Initial	0.407	0.740	0.457	0	0	0	0.510	-0.954
	Post-Processed	0.381	0.799	0.404	0	0	0	0.512	-0.954

similar response surface, providing the highest fitness improvement when the thickness in regions 7 to 9 is reduced. However, as seen in Figure 4, these regions are those where the lower boundary of the thickness is active. Therefore, due to the design constraints, such a modification would lead to unfeasible designs.

In addition, the sensitivity analysis can be used to remove complex features from the design. Thanks to the appropriate definition of the design space, the designs are already feasible but may contain features like the previously mentioned spikes in the thickness distribution. The sensitivity study allows to evaluate how removing these features would affect the final fitness.

The outcome of these post-processing steps is the *Post-processed* results in Figure 4 and Table 3. As can be observed, the thickness distribution becomes smoother and the fitness remains the same (0.1% improvement with respect to initial).

Finally, these new designs are fully evaluated to give a more detailed view of the results. First, Figure 6 presents the comparison between the objective shapes and the output shapes of the simulations. As can be observed, the designs accurately match the objective shapes, with a maximum difference of 0.2% of the chord with respect to the objective shape. Last Table 4 presents a summary of the worst failure indices, skin mass and actuator loads for each design. On the one hand, the failure indices for both materials are well below the acceptable limit of 0.66 ($1/SF$), which shows that the design is feasible for this application but, from a material allowables point of view, it is still possible to achieve higher deflections. On the other hand, the weight and actuator loads need to be considered together. The carbon fiber design is 13.5% lighter than the glass fiber one but the required actuator loads are 118% higher than the loads required by the glass fiber design. Therefore, even though the carbon fiber design is lighter, the mass penalty due to the actuation systems might be much higher, which would lead to an overall heavier design. For the next steps in this project, it is necessary to do a market search for actuators that could fit within the strut and then conduct a tradeoff study accounting not only for the skin weight but the full system weight.
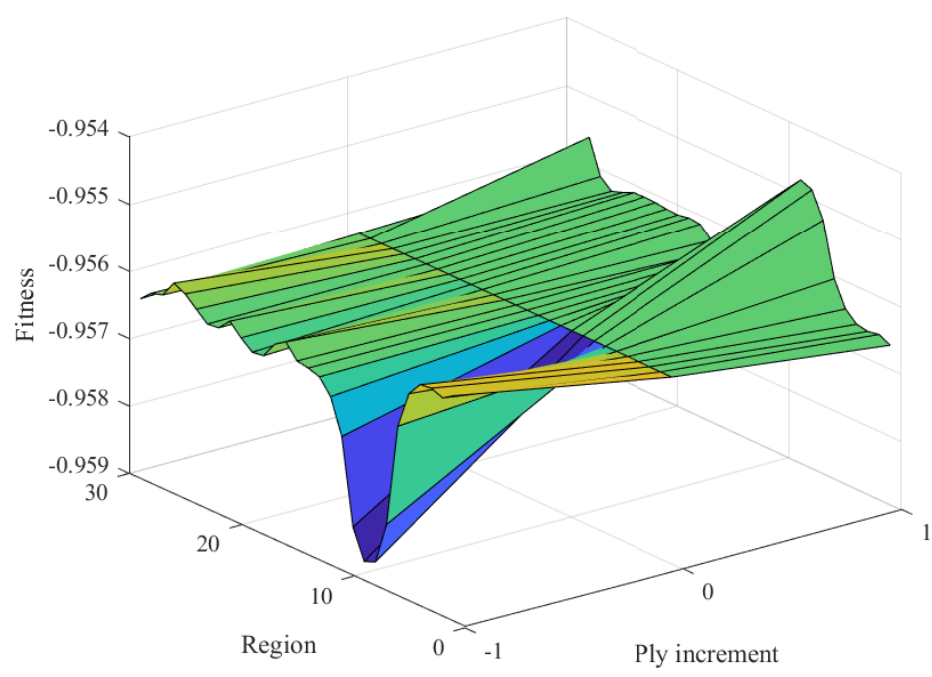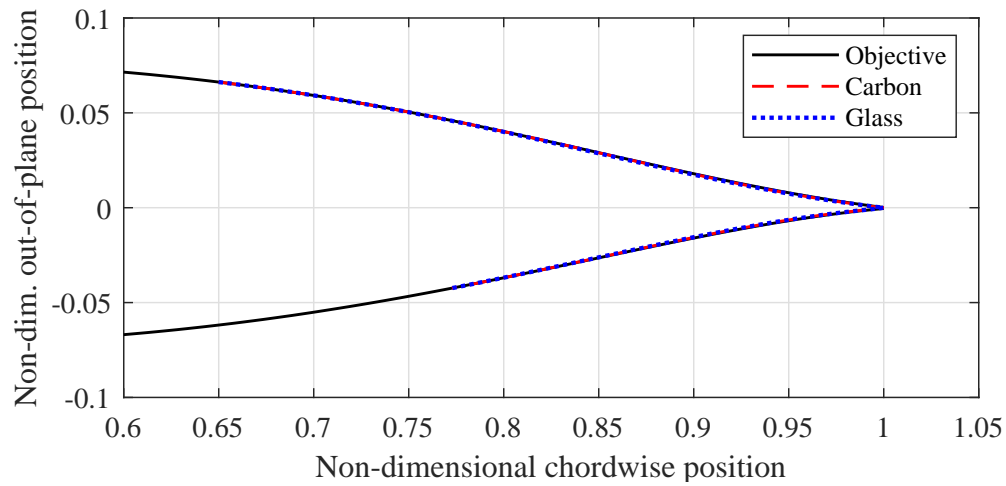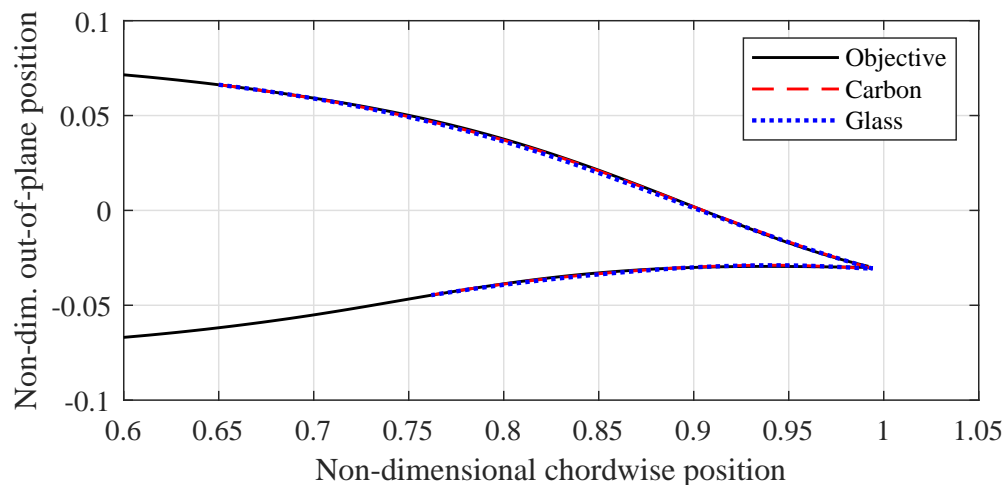
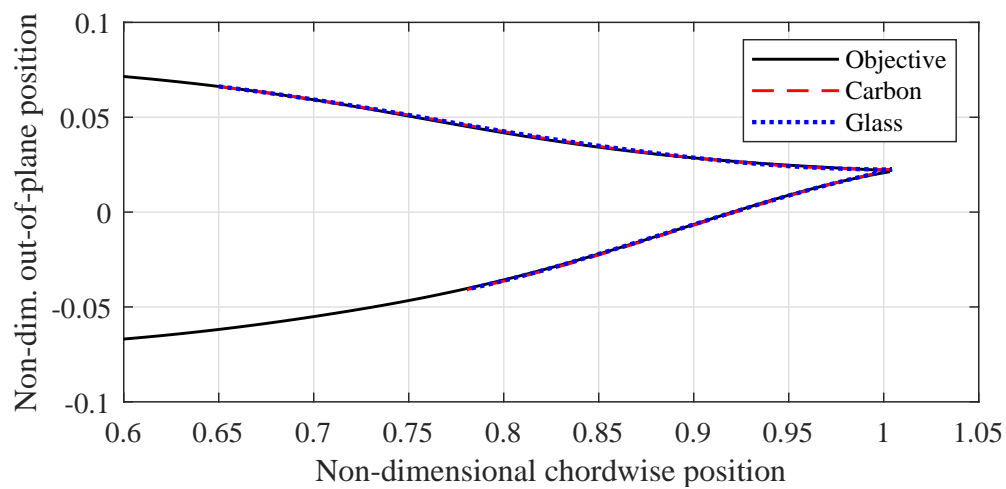**(a) Carbon**
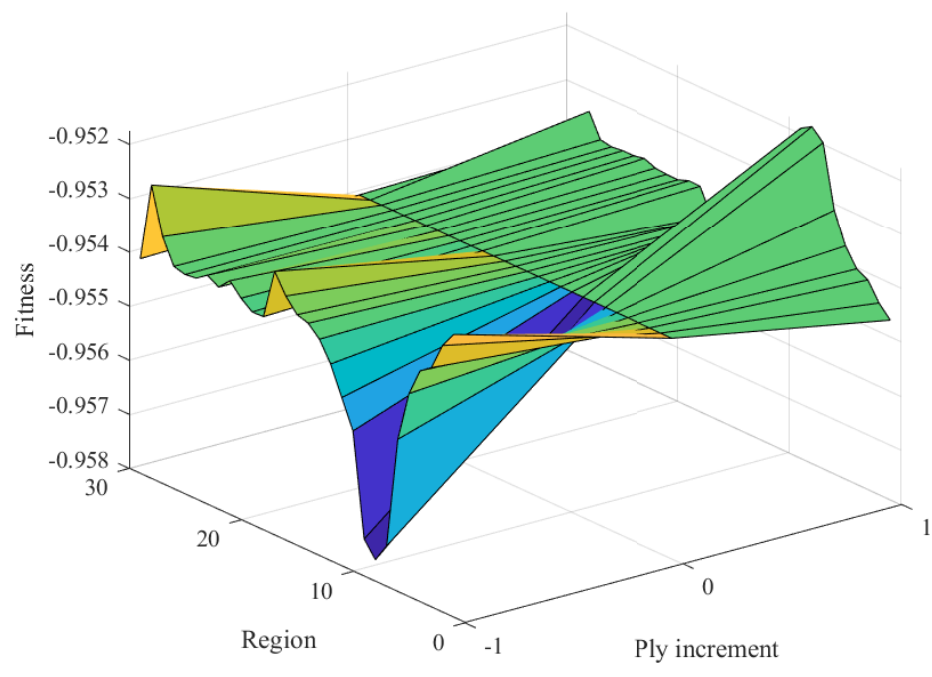
(b) Glass

Fig. 5   Fitness response surface for each material

8

(a) LC#1

(b) LC#2

(c) LC#3

Fig. 6   Comparison of objective shapes and actual shapes produced by the post-processed design of each material.

9

Table 4 Summary of strength, mass and actuator load assessment for each design.

Material	Worst Failure Index			Mass	Actuator Load
	LC#1	LC#2	LC#3	[kg/m]	[N/m]
Carbon	0.000	0.069	0.069	1.298	±1200
Glass	0.000	0.035	0.053	1.499	±550

IV. Conclusions

The presented study has focused on the structural sizing of a morphing trailing edge device implemented on the strut of a regional aircraft featuring a strut-braced wing. Considering a morphing design in which the upper skin is continuous and the lower skin can slide to provide the morphing, this study proposes an optimization framework to size the thickness of the skin. The objective of this optimization is to match the desired aerodynamic shapes while fulfilling manufacturing guidelines and constraints and minimizing the mass.

The optimizer computes the deflections and failure indices using NX Nastran and evaluates the fitness of the design using a weighted penalty approach. This fitness function is then fed to the Bayesian Optimization algorithm from Matlab to find the best design. Furthermore, a sensitivity analysis is used to evaluate the optimality of the designs and later refine them to remove unnecessary complex features.

The optimization is conducted using two different materials for the trailing edge skin: a carbon fiber and a glass fiber reinforced thermoplastic prepreg. For both materials, the optimizer finds designs showing good agreement with the objective shapes, with differences below 0.5% of the chord. In addition, the failure indices are well below the allowable, showing that there is still a margin for higher deflections if necessary.

Finally, this analysis can be used to make design decisions thanks to the mass and actuator loads predicted using the model. The carbon fiber design is lighter than the glass fiber but the required actuator loads are much higher. If only the skin mass was considered for the design, the carbon fiber design would be better. However, since the required loads are higher, bigger actuators would be required, leading to a mass penalty. For the final design, it is important to assess the design at the aircraft level, considering the aerodynamic benefits of morphing the strut in-flight and the possible weight and complexity penalties of including the morphing device.

In conclusion, this work has presented an optimization framework capable of sizing the morphing trailing edge skin to achieve the desired shapes at different flight conditions while already accounting for laminate manufacturing guidelines. Additionally, the laminate designs presented in this study will be used in the next steps of the HERWINGT project, in which the morphing strut will be mechanically tested to demonstrate the morphing capabilities of the concept.

Acknowledgements

References

[1] "What is ACARE?" ACARE, 2023. URL `https://www.acare4europe.org/about-us/`, [retrieved 10 May 2024].

[2] "Clean Aviation - History," Clean Aviation, 2024. URL `https://www.clean-aviation.eu/about-us/history`, [retrieved 10 May 2024].

[3] "Vision 2020: EASA presents its Vision for the Future of the Aviation Regulatory System," EASA, 2015. URL https://www.easa.europa.eu/en/newsroom-and-events/news/vision-2020-easa-presents-its-vision-future-aviation-regulatory-system, [retrieved 10 May 2024].

[4] European Commission, Directorate-General for Mobility and Transport and Directorate-General for Research and Innovation, *Flightpath 2050 - Europes vision for aviation: maintaining global leadership and serving societys needs*, Publications Office, 2012. https://doi.org/10.2777/15458.

[5] Anderson, J. D., *Fundamentals of aerodynamics*, 6th ed., McGraw Hill, New York, 2017, pp. 450–466.

[6] Gern, F. H., Naghshineh-Pour, A. H., Sulaeman, E., Kapania, R. K., and Haftka, R. T., "Structural Wing Sizing for Multidisciplinary Design Optimization of a Strut-Braced Wing," *Journal of Aircraft*, Vol. 38, No. 1, 2001, pp. 154–163. https://doi.org/10.2514/2.2747.

[7] Gur, O., Bhatia, M., Schetz, J. A., Mason, W. H., Kapania, R. K., and Mavris, D. N., "Design Optimization of a Truss-Braced-Wing Transonic Transport Aircraft," *Journal of Aircraft*, Vol. 47, No. 6, 2010, pp. 1907–1917. https://doi.org/10.2514/1.47546.

[8] Bhatia, M., Kapania, R. K., and Haftka, R. T., "Structural and Aeroelastic Characteristics of Truss-Braced Wings: A Parametric Study," *Journal of Aircraft*, Vol. 49, No. 1, 2012, pp. 302–310. https://doi.org/10.2514/1.C031556.

[9] Chakraborty, I., Nam, T., Gross, J. R., Mavris, D. N., Schetz, J. A., and Kapania, R. K., "Comparative Assessment of Strut-Braced and Truss-Braced Wing Configurations Using Multidisciplinary Design Optimization," *Journal of Aircraft*, Vol. 52, No. 6, 2015, pp. 2009–2020. https://doi.org/10.2514/1.C033120.

[10] Gupta, R., Schetz, J. A., and Kapania, R. K., "Conceptual Design of Complex Transonic Aircraft Configurations with Flutter Prediction," *58th AIAA/ASCE/AHS/ASC Structures, Structural Dynamics, and Materials Conference*, 2017. https://doi.org/10.2514/6.2017-0571.

[11] Droney, C. K., Sclafani, A. J., Harrisson, N. A., Grasch, A. D., and Beyar, M. D., "Subsonic Ultra-Green Aircraft Research Phase III: Mach 0.745 Transonic Truss-Braced Wing Design," Tech. rep., NASA, 2020. CR-2020-5005698.

[12] "Sustainable Flight Demonstrator Project," NASA, 2024. URL https://www.nasa.gov/directorates/armd/iasp/sfd/.

[13] Ivaldi, D., Secco, N. R., Chen, S., Hwang, J. T., and Martins, J. R. R. A., "Aerodynamic Shape Optimization of a Truss-Braced-Wing Aircraft," *16th AIAA/ISSMO Multidisciplinary Analysis and Optimization Conference*, 2015. https://doi.org/10.2514/6.2015-3436.

[14] Secco, N. R., and Martins, J. R. R. A., "RANS-Based Aerodynamic Shape Optimization of a Strut-Braced Wing with Overset Meshes," *Journal of Aircraft*, Vol. 56, No. 1, 2019, pp. 217–227. https://doi.org/10.2514/1.C034934.

[15] Carrier, G. G., Atinault, O., Dequand, S., Hantrais-Gervois, J., C.Liauzun, Paluch, B., Rodde, A., and Toussaint, C., "Investigation of a strut-braced wing configuration for future commercial aircraft," *28th Congress of the International Council of Aeronautical Sciences, ICAS 2012*, 2012.

[16] Moerland, E., Pfeiffer, T., Böhnke, D., Jepsen, J., Freund, S., Liersch, C. M., Chiozzotto, G. P., Klein, C., Scherer, J., Hasan, Y. J., and Flink, J., "On the Design of a Strut-Braced Wing Configuration in a Collaborative Design Environment," *17th AIAA Aviation Technology, Integration, and Operations Conference*, 2017. https://doi.org/10.2514/6.2017-4397.

[17] Carrier, G. G., Arnoult, G., Fabbiane, N., Schotte, J.-S., David, C., Defoort, S., Benard, E., and Delavenne, M., "Multidisciplinary analysis and design of strut-braced wing concept for medium range aircraft," *AIAA SCITECH 2022 Forum*, 2022. https://doi.org/10.2514/6.2022-0726.

[18] "Hybrid Electric Regional Wing Integration Novel Green Technologies - HERWINGT," Cordis, 2023. URL https://cordis.europa.eu/project/id/101102010, [retrieved 24 April 2023].

[19] Werter, N., Sodja, J., Spirlet, G., and Breuker, R. D., "Design and Experiments of a Warp Induced Camber and Twist Morphing Leading and Trailing Edge Device," *24th AIAA/AHS Adaptive Structures Conference*, 2016. https://doi.org/10.2514/6.2016-0315.

[20] Mkhoyan, T., Thakrar, N. R., Breuker, R. D., and Sodja, J., "Morphing wing design using integrated and distributed trailing edge morphing," *Smart Materials and Structures*, Vol. 31, No. 12, 2022, p. 125025. https://doi.org/10.1088/1361-665X/aca18b.

[21] Carrillo, X., Sodja, J., and Breuker, R. D., "Optimization Framework of a Ram Air Inlet Composite Morphing Flap," *10th ECCOMAS Thematic Conference on Smart Structures and Materials*, 2023, pp. 317–330. https://doi.org/10.7712/150123.9788.444474.

[22] "Bayesian Optimization Algorithm," MathWorks, 2024. URL https://nl.mathworks.com/help/stats/bayesian-optimization-algorithm.html.

[23] "Simcenter Nastran Software," Siemens PLM Software, 2024. URL https://plm.sw.siemens.com/en-US/simcenter/mechanical-simulation/nastran/.

[24] "Simcenter simulation and test solutions," Siemens PLM Software, 2024. URL https://plm.sw.siemens.com/en-US/simcenter/.

[25] Doyle, S., "pyNastran: A Python-based interface tool for Nastran's file formats," , 2020. URL https://github.com/SteveDoyle2/pyNastran, release 1.3.3.

[26] Tsatsas, I., Sticchi, E., Carrillo, X., Breuker, R. D., and Sodja, J., "Impact of Morphing Strut on Strut-Braced Wing Aerodynamic Efficiency," *AIAA SCITECH 2025 Forum*, 2025.

[27] "Toray Cetex TC1100 - Datasheet," , 2021. URL https://www.toraytac.com/product-explorer/products/u0I7/Toray-Cetex-TC1100.